U-Net-based Semantic Classification for Flood Extent Extraction using SAR Imagery and GEE Platform: A Case Study for 2019 Central US Flooding

Zhouyayan Li [a,b*], Ibrahim Demir [a,b]

[a] Department of Civil and Environmental Engineering, University of Iowa, Iowa City, Iowa, USA

[b] IIHR Hydroscience and Engineering, University of Iowa, Iowa City, Iowa, USA

* Corresponding Author, Email: zhouyayan-li@uiowa.edu

Abstract

Data-driven models for water body extraction have experienced accelerated growth in recent years, thanks to advances in processing techniques and computational resources, as well as improved data availability. In this study, we modified the standard U-Net, a convolutional neural network (CNN) method, to extract water bodies from scenes captured from Sentinel-1 satellites of selected areas during the 2019 Central US flooding. We compared the results to several benchmark models, including the standard U-Net and ResNet50, an advanced thresholding method, Bmax Otsu, and a recently introduced flood inundation map archive. Then, we looked at how data input types, input resolution, and using pre-trained weights affect the model performance. We adopted a three-category classification frame to test whether and how permanent water and flood pixels behave differently. Most of the data in this study were gathered and pre-processed utilizing the open access Google Earth Engine (GEE) cloud platform. According to the results, the adjusted U-Net outperformed all other benchmark models and datasets. Adding a slope layer enhances model performance with the 30m input data compared to training the model on only VV and VH bands of SAR images. Adding DEM and Height Above Nearest Drainage (HAND) model data layer improved performance for models trained on 10m datasets. The results also suggested that CNN-based semantic segmentation may fail to correctly classify pixels around narrow river channels. Furthermore, our findings revealed that it is necessary to differentiate permanent water and flood pixels because they behave differently. Finally, the results indicated that using pre-trained weights from a coarse dataset can significantly minimize initial training loss on finer datasets and speed up convergence.

Keywords: 2019 Central US floods, Google Earth Engine, U-Net, Bmax Otsu, Resnet, Sensitivity analysis, CNN

1. Introduction

Accurate flood maps are one of the most important and fundamental resources that aid operations during floods, such as rescue and evacuation (Benoudjit & Guida, 2019; Gebrehiwot & Hashemi-Beni, 2020), decision making (Ewing & Demir, 2021; Teague et al., 2021), and serve as the foundation for many secondary analyses, such as flood risk and loss analysis (Alabbad et al., 2021, 2022; Yildirim & Demir, 2021). High-quality data is one requirement for developing reliable flood extent predictions. Ground-based stream gauges, hydrometric stations, and field observations have traditionally been used as key data sources for flood simulation. However, many traditional data collection systems face challenges such as the high cost and labor required to maintain existing stations and keep up with the rapid needs for creating new data that matches the pace of other changes such as land use change (Muste et al., 2017; Pike et al., 2019; WMO, 2015). Among all prospective developments that may increase data availability in the future, two components stand out, notably, crowd-sourced data and remotely sensed imagery (Mignot & Dewals, 2022; Mishra et al., 2022). Although both can cover a large area rapidly, remotely sensed imagery has a significant advantage in terms of data accuracy and temporal and spatial consistency. Furthermore, remote sensing data can be utilized to generate new data, such as super-resolution DEMs (Demiray et al., 2021) and new satellite-based river imagery (Gautam et al., 2022). Additionally, remotely sensed data can provide estimates, such as precipitation (Seo et al., 2019) and sedimentation movements (Xu, Demir, et al., 2019; Xu, Muste, et al., 2019), that are hard to collect using other approaches. Previous research has demonstrated the utility of images captured by remote optical sensors such as Landsat, Sentinel-2, WorldView, and the Moderate Resolution Imaging Spectroradiometer (MODIS) in global forest canopy height measurement, agricultural detection and measurements, fire detection, Land Cover and Land Use (LULC) classification, and water body extraction (Abdi, 2020, Cheng et al., 2020, Jiang et al., 2021, Potapov et al., 2021). Although widely used in many aspects, optical images can be less favorable in water body extraction because one common disadvantage of passive sensors, including the ones mentioned above, is that they require a clear view with adequate illumination, which limits their applications during nights and in scenes where cloud is dominant (Yan et al., 2015).

Synthetic Aperture Radar (SAR) sensors, by contrast, are active sensors that capture signals sent out by the sensor itself, allowing them to work day and night and penetrate cloud coverage. Currently, the most widely utilized SAR data come from the European Space Agency's (ESA) Sentinel-1 satellite (Markert et al., 2020). SAR-based inundation mapping approaches can be divided into visual interpretation and digitization, threshold-based methods, change detection, supervised and unsupervised classifications, region expanding algorithms, and object-oriented image analysis techniques (Manavalan, 2017). Significant progress has been made in most of the aforementioned categories throughout the years (Li et al., 2018; Lu et al., 2014; Tiwari et al., 2020; Ye et al., 2021) as a result of improved data storing and processing techniques and data availability. Water extent extraction using machine learning (ML) and deep learning (DL) algorithms has experienced explosive growth in recent years (Yu Bai et al., 2022; Mishra et al., 2022; Sit, Demiray, et al., 2021; Xiang et al., 2021) in various application scenarios such as delineating wetland areas (Salehi et al., 2018), monitoring spatial-temporal changes (Kseňak et al., 2022), long-term change detection (Zhang et al., 2020), agricultural field mapping (T. Hu et al., 2021).

Although prior research obtained promising results utilizing ML and DL algorithms, many of them shared a similar issue that undermined the reliability of the results: a lack of comparison with enough benchmark datasets (Demir et al., 2022; Sit et al., 2021) and a lack of comparison with state-of-the-art benchmark models (Krajewski et al., 2021). For example, some previous studies failed to compare their results against sufficient models and methods (Tiampo et al., 2021; Xu et al., 2021), and some involve comparison with methods without considering recent advancements in those methods (Dong et al., 2021;

Katiyar et al., 2021; Wang et al., 2022), such as comparing against the standard Otsu thresholding algorithm rather than its latest advanced version, and the limited studies that involved comparisons with existing flood inundation maps created by others for the same area (Bai et al., 2021; Katiyar et al., 2021; Konapala et al., 2021). Sufficient comparisons are critical for flood inundation mapping using ML/DL models because, first, given the time and computing resources required by ML/DL models, we may prefer traditional methods if the performance difference between data-driven models and traditional methods is not significant. Currently, given that studies including comparison with refined traditional methods are few, and many of them compared the latest ML/DL model with traditional methods introduced decades ago without considering current developments in these approaches, their conclusions may be misleading. Second, the findings of ML/DL models are often highly sensitive to study regions, as evidenced by a study done by Sadiq et al. (2022) in which the validation results of the same model vary between 0.02 and 0.93 when the study area changes. As a result, multi-sourced benchmark datasets and models are required for validation before we can ascribe satisfactory outcomes to ML/DL models. Otherwise, the satisfying result could just be because the study region is easier to classify, implying that it may be possible that a far simpler strategy can get comparable results. The final issue yet to be adequately addressed is related to the data utilized for model training. ML/DL models excel at handling huge and complicated datasets. In contrast, in real-world applications, we may prefer to work with fewer inputs that produce acceptable outcomes when data availability, model portability, and data acquisition and processing costs are considered. However, sensitivity analysis on common data used in water extent extraction using ML/DL models is limited thus far.

To close those gaps, the first goal of this study is to apply a U-Net-based flood extent extraction framework to the 2019 Central US Flooding event and compare the results with two state-of-the-art DL models (ResNet50 and standard U-Net) that have been proven efficient in water body extraction. The results will also be compared with an advanced threshold-based method (Bmax Otsu) proposed in recent years and with flood extent maps created using the same data and kept in a recently introduced open-access flood map repository. Furthermore, we investigated the performance sensitivity of common data utilized in water body extraction, such as the Digit Elevation Model (DEM), slope, and Height Above Nearest Drainage (HAND), as well as the impact of data resolution and transfer learning.

2. Data and Methodology

2.1 Case Study - 2019 Central US Flooding

The 2019 Central US flooding was caused by a series of flooding events and storms that mostly occurred along the Missouri River and its tributaries in Nebraska, Iowa, Kansas, Missouri, and South Dakota. It began in the spring of 2019 with a mixture of rapid snow melting after the winter's record-breaking snowfall and high runoff from rain-on-snow occurrences (Flanagan et al., 2020). Due to the continuous rainstorms over the spring-summer season, the situation lasted for several months and resulted in an estimated economic loss of $3 billion, as stated by the Federal Emergency Management Agency in August 2019 (Flanagan et al., 2020; NASA, n.d.).

2.2 Data Preprocessing

Since the 2019 Central US Flooding was a massive event that lasted for a long time and affected considerably greater areas across numerous states than most local floods, after reviewing all accessible reference maps we chose the scenes captured by SAR on 05/22, 06/05, and 06/10, 2019 based on data coverage and quality. Figure 1 depicts the research area that each SAR image covers.

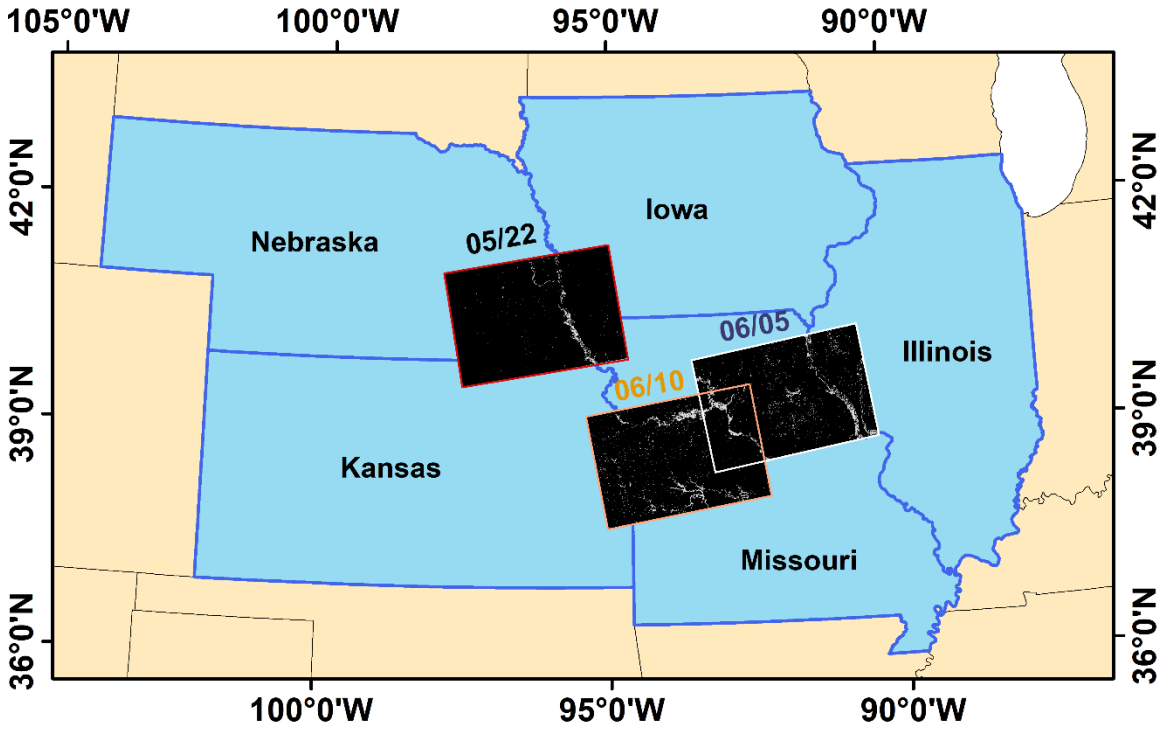

Figure 1. The study areas covered by SAR images captured on May 22, June 5 and 10, 2019

Table 1. Description of data used in this study

Item	Resolution	Collected Date	Data Source
Sentinel-1 GRD Imagery (VV+VH)	10m	05/22/2019, 06/05/2019, 06/10/2019	ESA[G]
DEM1	30m	-	NASA SRTM Digital Elevation 30 m (Farr et al., 2007)[G]
DEM2	10m	-	USGS 3DEP National Map Seamless 1/3 Arc-Second (USGS, n.d.)[G]
Slope1	30m	-	Derived from DEM1[G]
Slope2	10m	-	Derived from DEM2[G]
HAND Layer1	30m	-	Global 30m Height Above the Nearest Drainage (Donchyts et al., 2016)[G]
HAND Layer2	10m	-	Height Above Nearest Drainage (HAND) for CONUS (Y. Liu, 2018)
Bench Flood Maps	10m	Same dates as the Sentinel-1 Imagery	10m Flood Inundation Archive (2016-2019) from Sentinel-1 SAR Imagery over CONUS (Yang et al., 2021)
Reference Maps	30m	Same dates as the Sentinel-1 Imagery	NASA MSFC

G: Data that are pulled directly from Google Earth Engine platform

The reference maps used to evaluate model performance are ready-to-use flood extent maps in raster format created by NASA's Marshall Space Flight Center (MSFC) using data from the ESA Sentinel-1A satellite. Table 1 summarizes the key data sources used in this study. We selected DEM, slope ,and HAND layers as geomorphic elements that could potentially improve prediction performance in our work

because they are extensively employed in flood extent extraction (Aristizabal et al., 2020; Bosch et al., 2020). The HAND layer, like the DEM layer, gives a pixel-level description of the elevation difference between each pixel on the map and the nearest pixel in the drainage network to which the current pixel flows. Detailed introduction of the HAND index (Nobre et al., 2011; Rennó et al., 2008), comprehensive evaluation of HAND (Li et al., 2022), and web-based implementation (Hu & Demir, 2021) are available in the literature.

Google Earth Engine is a cloud-based platform targeted at supporting planetary-scale geospatial analysis (Gorelick et al., 2017). Since its introduction, it has substantially facilitated studies that require massive geo data and long-term environmental monitoring (Amani et al., 2020; Tamiminia et al., 2020). The two most important factors that made GEE popular in geospatial, hydrologic, and many other research fields include allowing free access to large-scale high-performance cloud computing resources and the integration of numerous public remote sensing and geospatial dataset worldwide. Some of the most frequently used data in GEE catalog are listed in the paper by Gorelick et al. (2017) and the list continues to increase on a daily basis as new data become available. In this study, we extracted various datasets from GEE directly, as shown in Table 1, and uploaded other items from local storage to GEE in TIFF format. The data will then be processed together in GEE, as shown in Figure 2.

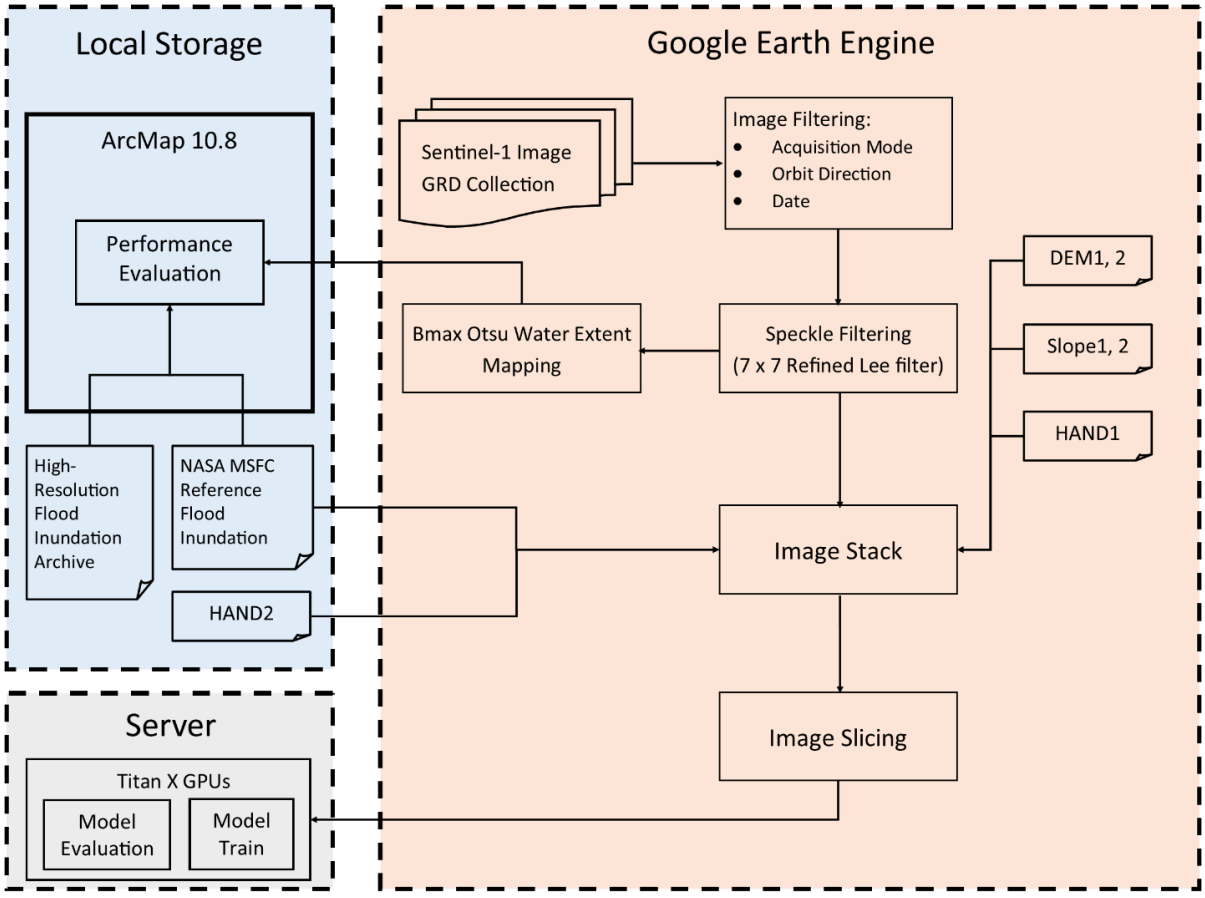

Figure 2. Data processing between phases in this study

We filtered SAR imagery based on event dates, Interferometric Wide (IW) acquisition mode, Ascending orbit direction, and resolution (10-m). For further details, readers are encouraged to check the Sentinel-1 SAR User Guide prepared by ESA for more information. In this study, the target SAR image is

a C-band ground range detected (Sentinel-1 SAR GRD) product with VV and VH bands on the GEE platform that has already undergone preprocessing steps such as orbit metadata update, ARD border noise removal, thermal noise removal, radiometric calibration, and terrain correction (Moothedan et al., 2020). As a result, the only pre-processing step left is to reduce speckle noise and increase coherency, for which we employed the Refined Lee filter (Lee et al., 2017). Following that, multiple data layers are stacked and then cut using the SAR image's scope. Finally, the clipped picture stacks and reference images are sliced into nonoverlapping patches and exported to local storage in TIFF format.

2.3 Benchmark Models and Dataset of the Study

Ronneberger et al. (2015) introduced U-Net, a deep convolutional neural network, for medical image semantic segmentation. Because of its precision and ability to deal with small datasets (Yan et al., 2022), it has been widely employed in several research domains, including remote-sensed image processing (Li et al., 2021; Zhang et al., 2021). In this study, we adopted the U-Net architecture described by Ronneberger et al., (2015) with the modification of employing a three-pixel kernel, one-pixel stride, and one-pixel padding to maintain the height and width of image patches between two consecutive convolution processes. ResNet is proposed by He et al. (2016) based on the idea of residual learning. ResNet50 is a ResNet version with 50 layers and 16 residual bottleneck blocks (Loey et al., 2021) and has also been widely used in studies related to water body extraction (Jain et al., 2020; Quan et al., 2020; Rambour et al., 2020; Salluri et al., 2020).

The Bmax Otsu algorithm was developed by Markert et al. (2020) as an adaptation of the automated segmentation-based thresholding method developed by Cao et al. (2019), which provided an iterative multi-scale selection strategy that addressed the issue where the original Otsu's bimodal assumption was not valid for the entire study scene. In this study, we refined the water body extracted by Bmax Otsu by removing pixels with slopes greater than 4°, fewer than 20 adjacent inundation neighbors, a HAND value greater than 10, and a frequency of occurrence greater than 5 months per year. All of those are common post-processing steps for threshold-based water extractions (Tsyganskaya et al., 2016; Tsyganskaya et al., 2018)

High-Resolution Flood Inundation Archive (referred to as FIA hereinafter) was developed by Yang et al. (2021) that contains nearly the entire Sentinel-1 SAR image archive from January 2016 to December 2019. This archive was created using a near-real-time inundation mapping system called Radar-Produced Inundation Diary (RAPID) developed by Shen et al. (2019). Yang et al. (2021) compared the inundation maps of their archive with the USGS Dynamic Surface Water Extent (DSWE) product and reported a substantial agreement between those two with an overall, user, producer agreements, and CSI of 99.06 %, 87.63%, 91.76%, and 81.23%.

2.4 Model Implementation

We adopted a three-category classification in which each pixel on a map is labeled as non-water, permanent (known) water, or floodwater. We selected the three-category classification frame rather than a two-category (water and non-water) classification frame because permanent water features, such as rivers and lakes, do not naturally distinguish themselves from floodwater. It takes more work to separate them distinctly, making a three-category classification more reasonable. Another factor to consider is that predictions for permanent water and flood water behaved differently, as demonstrated by prior studies that distinguished between permanent and flood water (Bai et al., 2021; Bonafilia et al., 2020; Katiyar et al., 2021). Therefore, water vs non-water classification will introduce bias into the results.

We combined image patches from the three flooding events and filtered all patches using a 0.1 threshold, which means that only patches with a ratio of water pixels (permanent + flood) over all pixels greater than 0.1 will be chosen as a sample for the model to train, validate and test. The reason for filtering image patches is that large-scale satellite images are known to be highly unbalanced for water body extraction problems (Bai et al., 2021), due to a notably greater number of non-water pixels than water pixels. This indicates that if image patches are not filtered, a significant amount of computing effort will be wasted predicting flood conditions for patches where almost all pixels are land or hillslope pixels. On the other hand, we do not recommend selecting a threshold that is too high as this may result in a too small sample population with insufficient image patches inside. Table 2 shows the settings for models with data resolutions of 10 and 30 m. Before settling on the current ones, we experimented with several hyperparameters such as batch size and epochs. In addition to the elements specified, we used random crop, horizontal and vertical flip to augment the data in both datasets. For model parameter updates and evaluation, we employed the Adam optimizer and a Cross-Entropy loss function.

Table 2. Model settings for 10- and 30-m resolution data

Resolution (m)	Total Patches	Patch Size (pixels)	Batch Size (patches)	Epochs	Data Division Ratio (Train:Validation:Test)
10	706	512 by 512	8	20	76:8:16
30	341	256 by 256	16	100	80:10:10

Our framework is built using PyTorch and trained on NVIDIA Titan X GPUs. We adopted the Cross-validation technique to make the most out of the training and validation sets (Molin et al., 2019). Previous research has shown that transfer learning can lead to faster convergence, smoother transplantation of a trained model to new datasets, and improved performance (Huang et al., 2020; Katiyar et al., 2021). Unlike the common practice of using off-the-shelf models trained by others on not-so-relevant datasets, we will use our model trained on 30m data as an initial state for training on data with a finer resolution of 10m.

2.5 Prediction Evaluation

Following the common practice of evaluating semantic classification (Bai et al., 2021; Bonafilia et al., 2020), we evaluated the model performance using mean Intersection over Union (mIoU) (averaging IoU of a certain class over all images), F1-score, and Overall Accuracy (OA) (averaging Accuracy over all images). Since we use a three-category classification, the mIoU and F1-score will be calculated for permanent water and flood water separately. Whereas the calculation of OA taking into account all three categories together.

$$IoU = \frac{Intersection\ between\ the\ reference\ and\ the\ model}{union\ of\ the\ reference\ and\ the\ model} = \frac{TP}{TP + FP + FN} \qquad Eq.(1)$$

$$F_1 = \frac{2 \times precision \times recall}{precision + recall} = \frac{TP}{TP + \frac{1}{2}(FP + FN)} \qquad Eq.(2)$$

$$Accuracy = \frac{TP + TN}{TP + FP + FN + TN} \qquad Eq.(3)$$

TP means the number of pixels belonging to the same class on both predicted and reference maps and TN means the number of pixels that are consistent on the predicted and reference maps but do not belong to the current category. FP means the number of pixels for which prediction believes they belong to the current class while they actually do not, and FN means the opposite of FP.

3. Results and Discussion

3.1 Performance Evaluation

Figure 3 illustrates the predicted flood inundation maps from ResNet50, standard U-Net, FIA, Bmax Otsu, and U-Net with 10-fold cross-validation and a few changed hyperparameters (hence referred to as adjusted U-Net) as explained in Section 2.4. Except for FIA and Bmax Otsu, all models are trained and tested using two-band picture patches with VV and VH bands. FIA images are classified maps ready for comparison. Bmax Otus water extent is calculated using the VV band because previous research has shown that the VV band is better suited for water extent mapping than the VH band (Agnihotri et al., 2019; Markert et al., 2020; Tiwari et al., 2020; Twele et al., 2016). The map created with Bmax Otsu underwent additional post-processing processes, as described in Section 2.3. It is worth noting that FIA categorizes pixels into only two types: non-water and water. As a result, blue pixels on FIA maps in Figure 3's last column reflect both flood pixels and permanent water pixels.

As shown in Figure 3, all models correctly predicted the flooding state for most pixels. Comparing the adjusted U-Net, normal U-Net, and ResNet50, it is clear that adjusted U-Net performs better in terms of maintaining the boundary shape of items on the map. Whereas the object boundary generated by ResNet50 is smoother, resulting in a moderate dilatation in water body extent, as demonstrated in scenes #8, #6, and #4. By contrast, because all of Bmax Otsu's processes are performed directly on the pixel level without any convolutional processes, it is able to maintain the most details at the pixel level. The pixel boundaries on Bmax Otsu maps are very sharp compared to the three DL models, allowing it to capture complex inundation conditions better, such as scene #3, where some isolated permanent water pixels are surrounded by flooded ones.

Keeping too many details, on the other hand, may make predictions "noisy" where pixels are less connected to other adjacent pixels in their group, make predictions less robust, and add difficulties in distinguishing between the two water categories and between permanent water and non-water classes, as in scene #4 where some permanent water on the right-hand side is misclassified as non-water and in scene #6 where some permanent water pixels in the meandering river network are misclassified as non-water. It is difficult to visually compare the FIA result with others because it does not distinguish between permanent and flood water. Although we can still discern when there appear to be far more water pixels than the label, as in scenes #6 at the top and #8 in the lower-left corner, or when there appear to be much less water pixels, as in scene #1. Therefore, a more quantitative comparison is required. The quantitative performance evaluation of each model/method described in Figure 3 is shown in Table 3.

In the last two rows, the mIoU and F1-score values are calculated without distinguishing between permanent and flood water so that they can be compared to the FIA results. Table 3 shows that the adjusted U-Net beats all other models and approaches. Except for FIA, we found that flood pixels have higher mIoU and F1-score values than permanent water pixels despite the models we used. Many prior studies have also revealed a difference in prediction performance between flood and permanent water (Bai et al., 2021; Bonafilia et al., 2020; Katiyar et al., 2021).

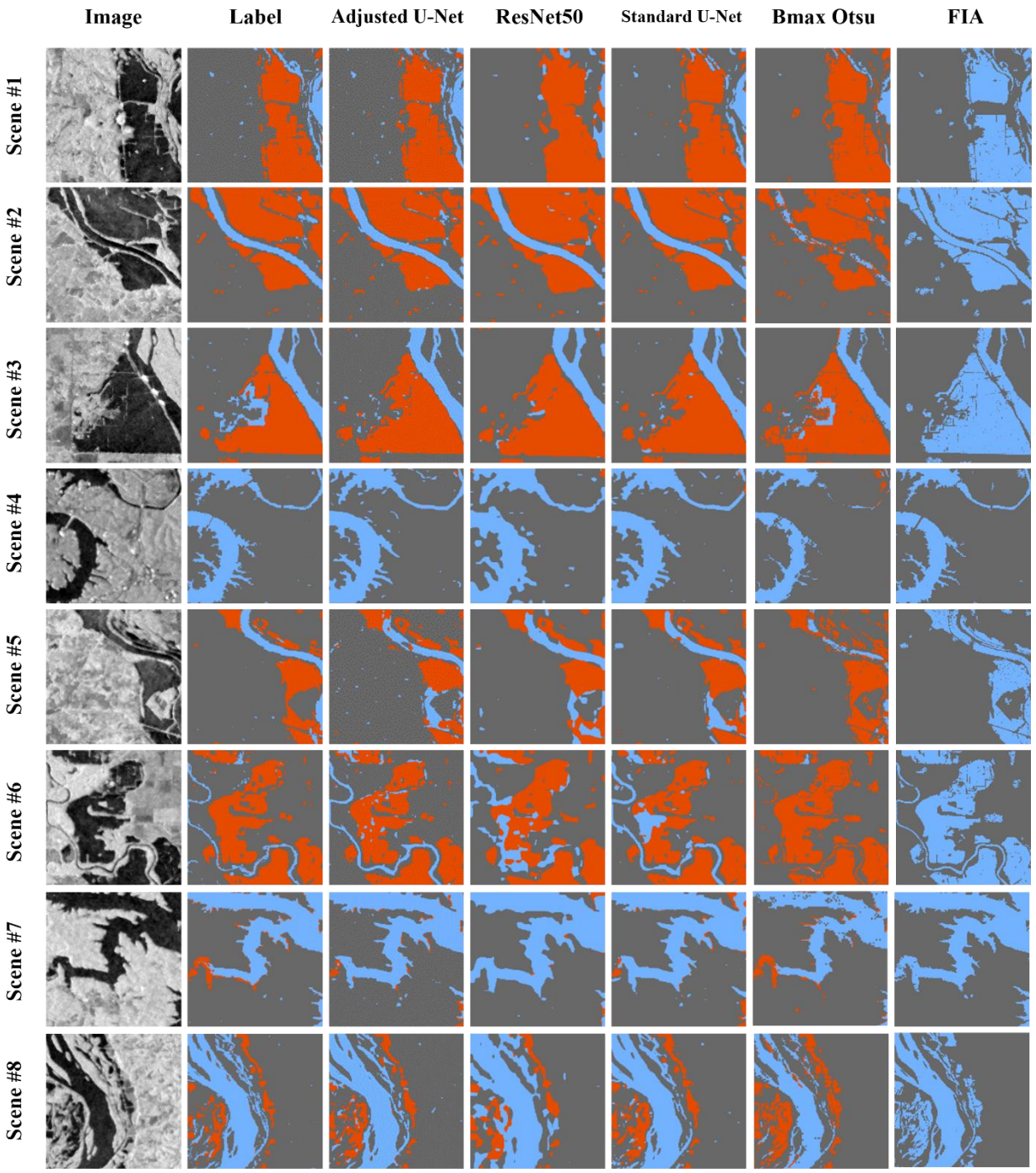

Figure 3. The inundation extent from three DL models, a thresholding method, and a benchmark dataset. The blue, red, and gray pixels represent permanent water, flood areas, and dry regions for all model predictions except for FIA (the last column) where the blue pixels are water bodies combining both permanent water and flood pixels

We, therefore, believe it is necessary to treat permanent and floodwater as separate classes, not only because of the inherent difference between them, but also because treating all water pixels as a whole may result in failure to reflect the actual prediction performance of either class, as shown in Table 3.

Additionally, we discovered that OA values are larger compared to other indices in the same column for all situations reported in Table 3. We believe this is because accuracy is skewed toward the number of dry pixels on most SAR images, which is disproportionally big compared to the number of water pixels. As a result, it necessitates the use of multiple evaluation indices concurrently, to include less biased indexes such as IoU, or to evaluate predictions of water and non-water pixels independently.

Table 3. Quantitative evaluation of models/methods shown in Figure 3

	Adjusted U-Net	ResNet50	Standard U-Net	Bmax Otsu	FIA
mIoU (Flood)	0.756	0.579	0.734	0.641	-
mIoU (Permanent)	0.667	0.503	0.662	0.631	-
F1-Score (Flood)	0.859	0.730	0.844	0.781	-
F1-Score (Permanent)	0.799	0.667	0.796	0.774	-
OA	0.924	0.851	0.919	0.890	0.924
mIoU (Water)	0.832	0.687	0.829	0.638	0.756
F1-Score (Water)	0.908	0.815	0.907	0.779	0.861

Figure 4 depicts the loss and accuracy curves for the standard (Figure 4 a) and the adjusted U-Net (Figure 4 b) during training and validation. We see that the standard U-Net begins to overfit after only 20 epochs, whereas the altered U-Net shows no obvious tendency of overfitting throughout the training process. Furthermore, there is less variation in loss and accuracy, particularly for the loss during the training phase, as demonstrated in Figure 4 (b) when cross-validation is applied. Because all the other hyperparameters in the two models are the same, the more stable training and validation processes, as well as the performance gain reported in Table 3, are due to the use of cross-validation.

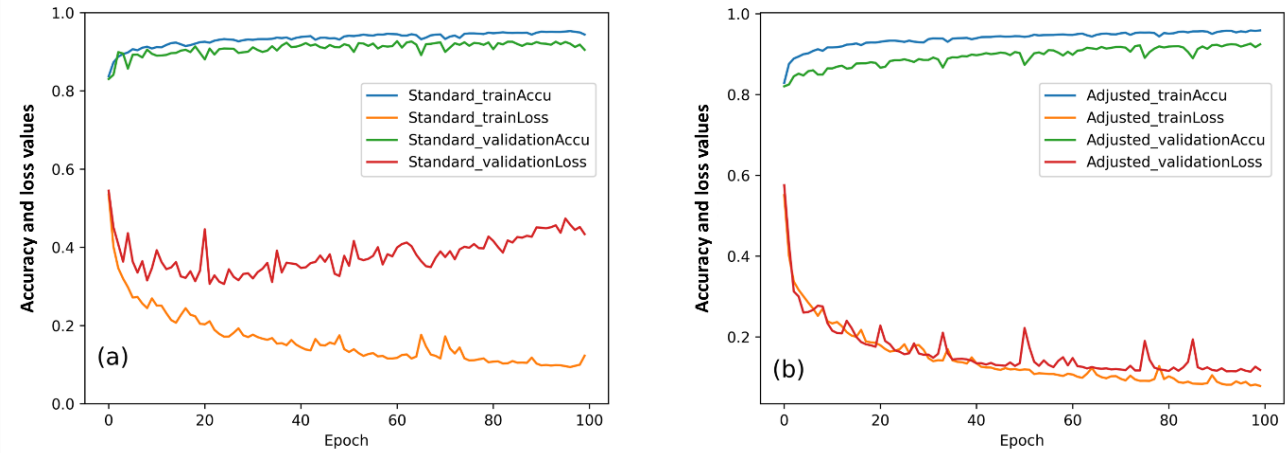

Figure 4. Changes in loss and accuracy (referred to as Accu in figure) over 100 epochs for the standard U-Net (a) and adjusted U-Net (b) trained on VV+VH

3.2 Performance of Adjust U-Net with Various Inputs

Figure 5 shows the inundation extent predictions using adjusted U-Net but with different input layers. The differences between label images and U-Net flood extent estimates with VV+VH+slope, VV+VH+slope+DEM, and VV+VH+slope+DEM+HAND are nuanced in most situations, as illustrated in Figure 5. Moderate differences are mostly found near the small groups of isolated pixels at the top of scenes #1 and #6, as well as the permanent water pixels surrounded by flooded pixels in scene #3. The other two configurations trained on three-band images, namely VV+VH+DEM and VV+VH+HAND,

failed to predict as accurately as the one with an additional slope band as we can see that there are noticeable mismatches, especially in scenes #3, #5, and #6. Table 4 summarized the quantitative evaluation of the model configurations stated previously.

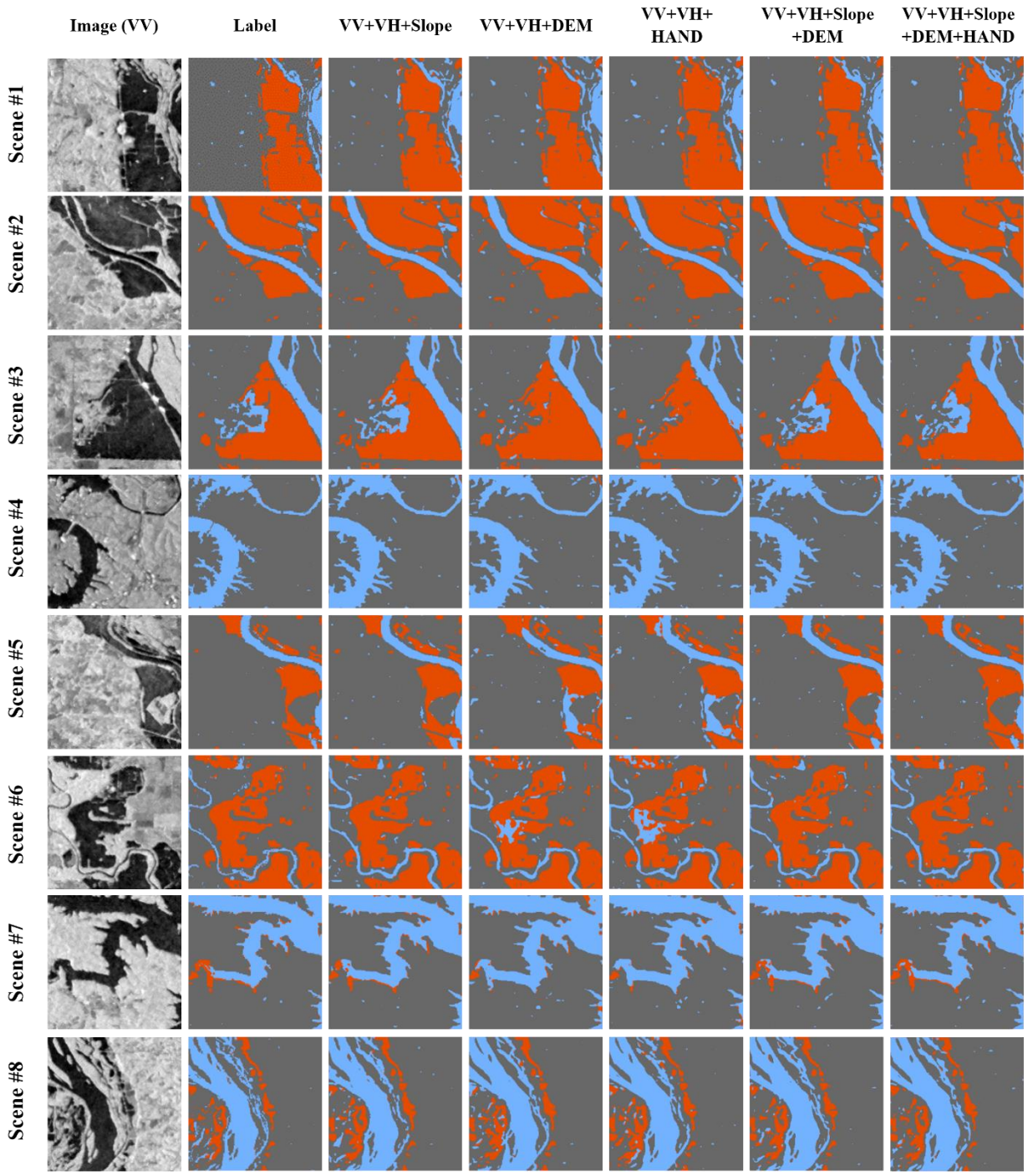

Figure 5. Inundation extent generated by adjusted U-Net trained on image samples with various layers. The blue, red, and gray pixels represent permanent water, flood areas, and dry regions.

Table 4. Evaluation model performance for adjusted U-Net with different image inputs

	VV+VH	VV+VH +Slope	VV+VH +DEM	VV+VH +HAND	VV+VH+ Slope+DEM	VV+VH+Slope +DEM+HAND
mIoU (Flood)	0.756	0.794	0.755	0.749	0.798	0.792
mIoU (Permanent)	0.667	0.744	0.674	0.683	0.751	0.741
F1-Score (Flood)	0.859	0.883	0.858	0.854	0.885	0.882
F1-Score (Permanent)	0.799	0.853	0.804	0.811	0.857	0.851
OA	0.924	0.935	0.924	0.925	0.937	0.933
mIoU (Water)	0.832	0.843	0.837	0.835	0.848	0.844
F1-Score (Water)	0.908	0.915	0.911	0.910	0.918	0.915

As shown in Table 4, training on three-band images with the slope as an additional data layer brings significant improvements for all listed indexes. While using a DEM or a HAND layer in addition to the two SAR signal bands does not result in a significant improvement for all indexes, we do see an increase in mIoU and F1-score for permanent water. Speaking of results trained with three data layers in permanent water areas, the one with an additional HAND layer shows slightly more improvements than results with an additional DEM layer. We believe that this is because DEM values are usually relative numbers against a specific datum, whereas HAND values are normalized elevations focusing on the relationship between any pixel and its nearest neighbor in drainage networks and are thus independent of datums. For all stream pixels, a HAND value of zero will make them easier to be recognized by DL models. For flood pixels, we discovered that there are also minor discrepancies between the results of the HAND input and the DEM input, where the latter leads to a slightly better prediction. Different from previous studies that reported considerable performance improvements with HAND as a side channel (Bosch et al., 2020), our results indicated that adding a HAND layer may not be beneficial in all cases. This could be due to the HAND characteristics of our study location. Many previous studies used HAND as a stand-alone model for flood inundation mapping and discovered that, while it can generate accurate flood extent predictions in many cases, it can also introduce a lot of mismatches in locations where the study area is flat (Jafarzadegan & Merwade, 2017, 2019; Samela et al., 2017) or the water depth of the entire area is not representative enough of small catchments inside the study area (Z. Li & Demir, 2022). Some recent research has also raised concerns about the uncertainty HAND would introduce within flat areas to remote sensing applications, which could compromise model accuracy (Liu et al., 2020). Finally, comparing results trained on three-band images with a slope layer to those trained on four-band and five-band images shows that adding more data does not improve performance in this case, making the three-band image the best input because it ensures similar predictions while requiring less data-processing and computational effort.

3.3 Flood Extent with a Finer Data Resolution

Figure 6 depicts the inundation extent predictions with adjusted U-Net trained on 10-m image patches with three bands (VV+VH+slope) and five bands (VV+VH+slope+HAND+DEM). Except for some scenes with complicated patterns, such as #3 and #1, it is difficult to identify the difference between predictions based on distinct inputs visually for most pixels among patches exhibited, as seen in Figure 6. When the river channels are narrow, like in scene #7, and the narrower branches in scenes #6, #5, and #4, dry pixels around the actual river channel can be misclassified into water pixels. This supports recent findings in which the authors claimed that CNN-based DL models, such as U-Net and DeepLabV3+ (Verma et al., 2021), failed to accurately extract narrow rivers captured by SAR images (Gasnier et al., 2021; Gasnier et al., 2021).

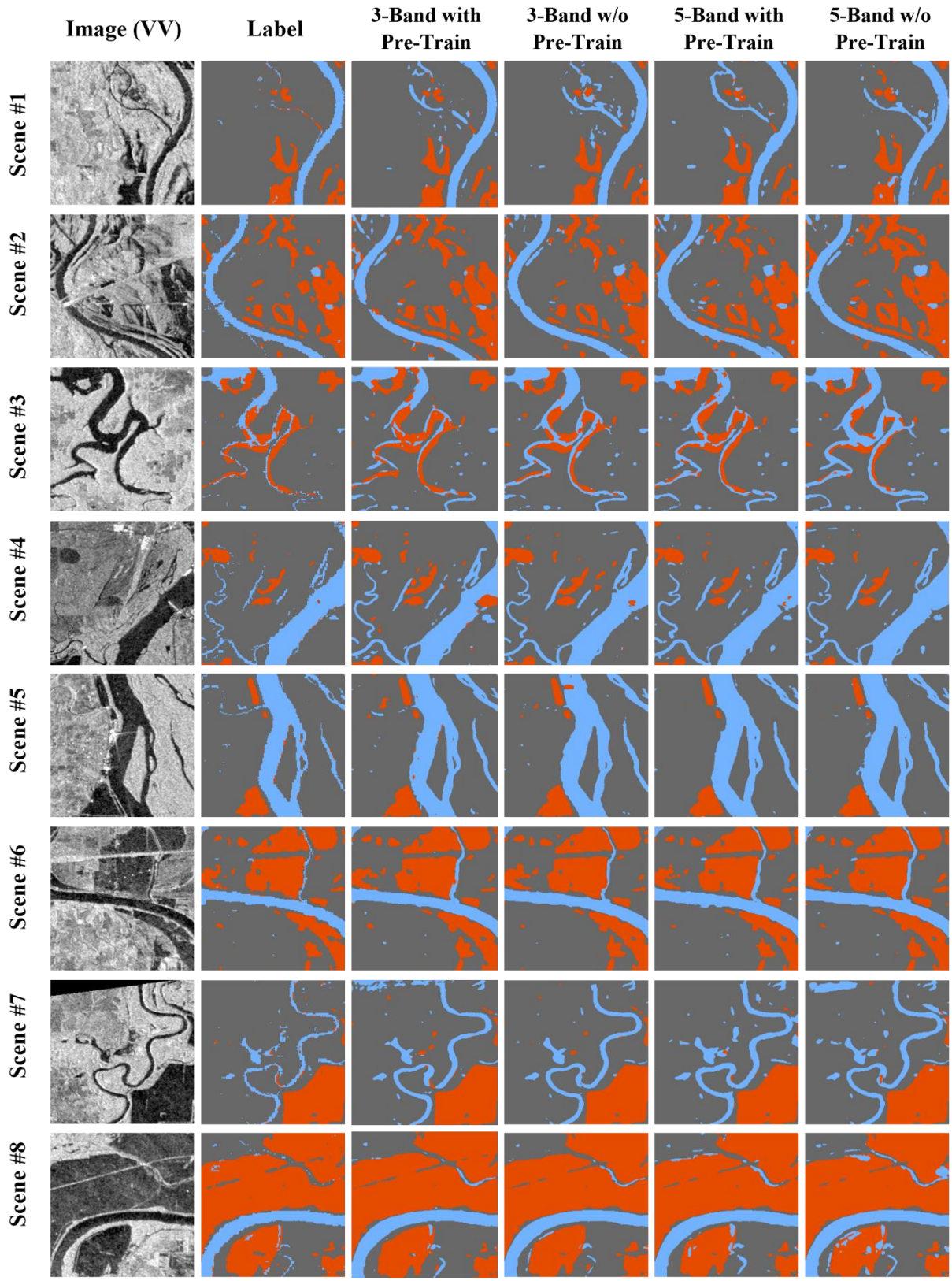

Figure 6. Water extent extraction with adjusted U-Net trained on 10-m image inputs. The blue, red, and gray pixels represent permanent water, flood areas, and dry regions

Some previous studies have attributed this issue to inherent speckle fluctuation in SAR images (Gasnier et al., 2021; Gasnier et al., 2021; Moharrami et al., 2021) but we believe it is also due to the mechanism of U-Net and other similar CNN-based semantic segmentation DL models, which down-sample images several times to extract abstract features (Guo et al., 2022) on images at the expense of reducing image resolution and then restores to the previous resolution by up-sampling. This down- and up-sampling will inevitably lose some details from the original images, result in the smoothing effect seen in Figure 3, and lead to the slight dilatation for narrow water channels.

Table 5 summarizes the performance evaluation of the model configurations depicted in Figure 6, as well as the one trained on 30-m resolution with three bands (VV+VH+slope). The other four trained on 10-m resolution data exhibited enhanced performance to varying degrees when compared to the one trained on 30-m resolution images. Although the data source for the two DEM layers is not the same, we believe the performance difference is primarily due to the finer data resolution. This is because they are both obtained from US federal agencies and have been widely used in previous studies (Oh et al., 2022; Scott et al., 2022; Uuemaa et al., 2020; Wong et al., 2020), and thus even if there are slight vertical differences between these two products, it is less likely that one has significantly higher data accuracy than the other. We discovered that the 10m three-band model without pretrain outperformed the outcomes of the five-band 10m model without pretrain.

Given that the training loss of both configurations is relatively high when compared to those with pre-trained weights as shown in Figure 7, we believe both models were under-trained, in which case the one with more data may perform worse because there are more uncertainties coming from a yet-to-be-built relationship between more variables and the outcome. Surprisingly, when we compared the three-band model to the five-band model, both with pre-trained weights, we discovered that the five-band model performed better in classifying flood pixels while the three-band achieved higher indexes for permanent water pixels, whereas the synthetic indexes (OA, mIoU, and F1-score) over all water pixels did not show a significant difference. When we compare results for models with the same input (with and without pre-train) we discovered that indexes increased to some extent for both flood and permanent water pixels for pre-trained models, but this difference is less significant for synthetic OA, mIoU, and F1-Score that were calculated without distinguishing between flood and permanent water pixels.

Table 5. Evaluation model performance for adjusted U-Net with different image inputs

	VV+VH+ Slope (30m)	VV+VH+Slope w/ Pretrain (10m)	VV+VH+Slope w/o Pretrain (10m)	VV+VH+Slope+ HAND+DEM w/ Pretrain (10m)	VV+VH+Slope+ HAND+DEM w/o Pretrain (10m)
mIoU (Flood)	0.794	0.850	0.840	0.857	0.819
mIoU (Permanent)	0.744	0.765	0.761	0.750	0.744
F1-Score (Flood)	0.883	0.918	0.912	0.922	0.899
F1-Score (Permanent)	0.853	0.865	0.863	0.856	0.851
OA	0.935	0.951	0.949	0.950	0.941
mIoU (Water)	0.843	0.875	0.869	0.875	0.859
F1-Score (Water)	0.915	0.934	0.930	0.933	0.924

The training loss with and without pre-trained weights is depicted in Figure 7. The loss curves demonstrate no substantial variation in patterns over training iterations (epochs), yet pre-trained models have a much lower initial loss than those trained from scratch. Furthermore, the loss values of the two with pre-training were approximately 40% lower than the others at the final epoch. The training losses at

epoch 20 for models with pre-trained weights in Figure 7 are very close to the final loss shown Figure 4 (b) for models trained over 100 epochs, whereas the two models without pre-trained weights require more iterations to further reduce the loss. It took roughly 40 minutes to iterate over one epoch with five-layer photos with 10-m resolution in our example, however it only took about 10 minutes to loop over an epoch with 30-m data with the same layers. Therefore, it is more efficient to apply a pre-trained model from coarse data to finer datasets rather than to train the model from scratch.

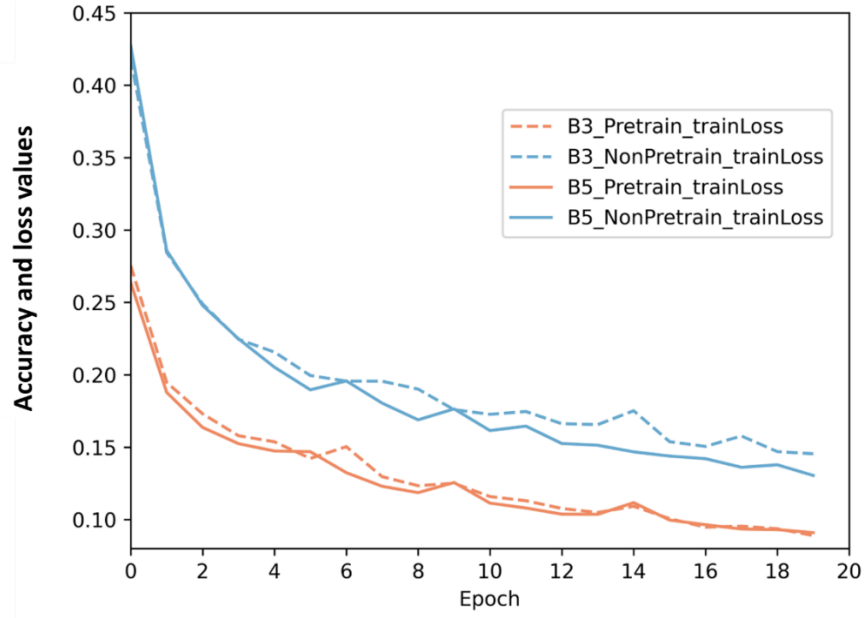

Figure 7. The training loss curves for models trained on the three- (B3) and five-band (B5) images with/without pre-train

4. Conclusion

In this study, we used a three-category classification to extract water bodies captured by the ESA Sentinel-1 satellites on May 22, June 5, and June 10, 2019, during the 2019 Central US flooding. We modified the conventional U-Net using moderately refined hyperparameters and 10-fold cross-validation. The adjusted U-Net was compared against the standard U-Net and ResNet50, as well as an advanced threshold-based technique, Bmax Otsu, and a newly introduced flood map archive derived from the same SAR images. The results demonstrated that the proposed adjusted U-Net model can extract water bodies more precisely than those benchmark models and approaches. The results of testing adjusted U-Net on 30m input layers revealed that adding DEM or HAND layers has limited effects on improving predictions when compared to the slope layer. The adjusted model was then trained using 10m image stacks with three (VV, VH, slope) and five data (VV, VH, slope, DEM, HAND) layers, and the performance was compared between models using previously trained weights on 30m input as initial weights and those trained from scratch. The results show that initializing the new model using pre-trained weights from a coarse dataset not only allows a considerably reduced initial training loss on the new dataset, but also speeds up convergence within a limited number of training iterations. Those trained from scratch, on the other hand, require more iterations to get the same results. As a result, we feel it is worthwhile to consider transferring pre-trained weights to new training on finer datasets for improved performance and training efficiency.

In addition to the results indicated above, our findings confirmed that prediction accuracy for permanent water and flood pixels varies among model settings, data utilized for prediction, and whether the model contains pre-trained weights. However, the differences among various model configurations were not as pronounced in synthetic indices that do not distinguish between permanent water and flood pixels. For future water body extraction studies, we suggest the three-class categorization instead of the two-class classification (water and non-water). Furthermore, ResNet50 and U-Net result images showed smoothed pixel boundaries and moderate water body dilation for narrow river channels compared to those on reference maps and the other two benchmark maps. This could be attributed to the inherent speckle fluctuation on SAR images but is more likely due to image detail loss during the down-sampling/up-sampling process or the convolution process that changes the image size.

Further research could investigate the mechanisms underlying the varied behavior of flood and permanent water pixels and try to design better model configurations that predict both classes more accurately. Another future direction might focus on enhancing the design of semantic segmentation DL models so that they can retain pixel boundaries better and do not cause considerable water scope dilation in narrow river channels.

Acknowledgement

We would like to acknowledge Ms. Lori A. Schultz and her colleagues at NASA's Marshall Space Flight Center of providing the reference flood inundation extent maps for this study.

References

Abdi, A. M. (2020). Land cover and land use classification performance of machine learning algorithms in a boreal landscape using Sentinel-2 data. *GIScience and Remote Sensing*, *57*(1), 1–20. https://doi.org/10.1080/15481603.2019.1650447/SUPPL_FILE/TGRS_A_1650447_SM9050.PDF

Agnihotri, A. K., Ohri, A., Gaur, S., Shivam, Das, N., & Mishra, S. (2019). Flood inundation mapping and monitoring using SAR data and its impact on Ramganga River in Ganga basin. *Environmental Monitoring and Assessment*, *191*(12), 1–16. https://doi.org/10.1007/s10661-019-7903-4

Alabbad, Y., Mount, J., Campbell, A. M., & Demir, I. (2021). Assessment of transportation system disruption and accessibility to critical amenities during flooding: Iowa case study. *Science of The Total Environment*, *793*, 148476. https://doi.org/10.1016/J.SCITOTENV.2021.148476

Alabbad, Y., Yildirim, E., & Demir, I. (2022). Flood mitigation data analytics and decision support framework: Iowa Middle Cedar Watershed case study. *Science of The Total Environment*, *814*, 152768. https://doi.org/10.1016/J.SCITOTENV.2021.152768

Amani, M., Ghorbanian, A., Ahmadi, S. A., Kakooei, M., Moghimi, A., Mirmazloumi, S. M., Moghaddam, S. H. A., Mahdavi, S., Ghahremanloo, M., Parsian, S., Wu, Q., & Brisco, B. (2020). Google Earth Engine Cloud Computing Platform for Remote Sensing Big Data Applications: A Comprehensive Review. *IEEE Journal of Selected Topics in Applied Earth Observations and Remote Sensing*, *13*, 5326–5350. https://doi.org/10.1109/JSTARS.2020.3021052

Aristizabal, F., Judge, J., & Monsivais-Huertero, A. (2020). High-resolution inundation mapping for heterogeneous land covers with synthetic aperture radar and terrain data. *Remote Sensing*, *12*(6), 900. https://doi.org/10.3390/rs12060900

Bai, Yanbing, Wu, W., Yang, Z., Yu, J., Zhao, B., Liu, X., Yang, H., Mas, E., & Koshimura, S. (2021). Enhancement of detecting permanent water and temporary water in flood disasters by fusing sentinel-1 and sentinel-2 imagery using deep learning algorithms: Demonstration of sen1floods11 benchmark datasets. *Remote Sensing*, *13*(11), NA. https://doi.org/10.3390/rs13112220

Bai, Yu, Zhao, Y., Shao, Y., Zhang, X., & Yuan, X. (2022). Deep learning in different remote sensing image categories and applications: status and prospects. *International Journal of Remote Sensing*,

43(5), 1800–1847. https://doi.org/10.1080/01431161.2022.2048319
Benoudjit, A., & Guida, R. (2019). A novel fully automated mapping of the flood extent on sar images using a supervised classifier. *Remote Sensing*, *11*(7), 779. https://doi.org/10.3390/rs11070779
Bonafilia, D., Tellman, B., Anderson, T., & Issenberg, E. (2020). Sen1Floods11: A georeferenced dataset to train and test deep learning flood algorithms for sentinel-1. *IEEE Computer Society Conference on Computer Vision and Pattern Recognition Workshops*, *2020-June*, 835–845. https://doi.org/10.1109/CVPRW50498.2020.00113
Bosch, M., Conroy, C., Ortiz, B., & Bogden, P. (2020). Improving emergency response during hurricane season using computer vision. *Earth Resources and Environmental Remote Sensing/GIS Applications XI*, *11534*, 14. https://doi.org/10.1117/12.2574639
Cao, H., Zhang, H., Wang, C., & Zhang, B. (2019). Operational Flood Detection Using Sentinel-1 SAR Data over Large Areas. *Water 2019, Vol. 11, Page 786*, *11*(4), 786. https://doi.org/10.3390/W11040786
Cheng, T., Ji, X., Yang, G., Zheng, H., Ma, J., Yao, X., Zhu, Y., & Cao, W. (2020). DESTIN: A new method for delineating the boundaries of crop fields by fusing spatial and temporal information from WorldView and Planet satellite imagery. *Computers and Electronics in Agriculture*, *178*, 105787. https://doi.org/10.1016/J.COMPAG.2020.105787
Demir, I., Xiang, Z., Demiray, B., & Sit, M. (2022). *WaterBench: A Large-scale Benchmark Dataset for Data-Driven Streamflow Forecasting*. *March*, 1–19. https://doi.org/https://doi.org/10.5194/essd-2022-52
Demiray, B.Z., Sit, M., & Demir, I. (2021). D-SRGAN: DEM Super-Resolution with Generative Adversarial Networks. *SN Computer Science*, *2*(1), 1–11. https://doi.org/10.1007/s42979-020-00442-2
Donchyts, G., Winsemius, H., Schellekens, J., Erickson, T., Gao, H., Savenije, H., & van de Giesen, N. (2016). Global 30m Height Above the Nearest Drainage. *EGUGA*, *18*, EPSC2016-17445. https://doi.org/10.13140/RG.2.1.3956.8880
Dong, Z., Wang, G., Amankwah, S. O. Y., Wei, X., Hu, Y., & Feng, A. (2021). Monitoring the summer flooding in the Poyang Lake area of China in 2020 based on Sentinel-1 data and multiple convolutional neural networks. *International Journal of Applied Earth Observation and Geoinformation*, *102*, 102400. https://doi.org/10.1016/J.JAG.2021.102400
Ewing, G., & Demir, I. (2021). An ethical decision-making framework with serious gaming: a smart water case study on flooding. *Journal of Hydroinformatics*, *23*(3), 466–482. https://doi.org/10.2166/HYDRO.2021.097
Farr, T. G., Rosen, P. A., Caro, E., Crippen, R., Duren, R., Hensley, S., Kobrick, M., Paller, M., Rodriguez, E., Roth, L., Seal, D., Shaffer, S., Shimada, J., Umland, J., Werner, M., Oskin, M., Burbank, D., & Alsdorf, D. E. (2007). The shuttle radar topography mission. *Reviews of Geophysics*, *45*(2). https://doi.org/10.1029/2005RG000183
Flanagan, P. X., Mahmood, R., Umphlett, N. A., Haacker, E., Ray, C., Sorensen, W., Shulski, M., Stiles, C. J., Pearson, D., & Fajman, P. (2020). A Hydrometeorological Assessment of the Historic 2019 Flood of Nebraska, Iowa, and South Dakota. *Bulletin of the American Meteorological Society*, *101*(6), E817–E829. https://doi.org/10.1175/BAMS-D-19-0101.1
Gasnier, N., Dalsasso, E., Denis, L., & Tupin, F. (2021). Despeckling Sentinel-1 GRD Images by Deep-Learning and Application to Narrow River Segmentation. *2021 IEEE International Geoscience and Remote Sensing Symposium IGARSS*, 2995–2998. https://doi.org/10.1109/igarss47720.2021.9554350
Gasnier, N., Denis, L., Fjortoft, R., Liege, F., & Tupin, F. (2021). Narrow River Extraction from SAR Images Using Exogenous Information. *IEEE Journal of Selected Topics in Applied Earth Observations and Remote Sensing*, *14*, 5720–5734. https://doi.org/10.1109/JSTARS.2021.3083413
Gautam, A., Sit, M., & Demir, I. (2022). Realistic River Image Synthesis Using Deep Generative Adversarial Networks. *Frontiers in Water*, *4*. https://doi.org/10.3389/frwa.2022.784441
Gebrehiwot, A., & Hashemi-Beni, L. (2020). A METHOD TO GENERATE FLOOD MAPS IN 3D USING DEM AND DEEP LEARNING. *The International Archives of the Photogrammetry, Remote*

Sensing and Spatial Information Sciences, *XLIV-M-2–2*, 25–28. https://doi.org/10.5194/isprs-archives-xliv-m-2-2020-25-2020

Giglio, L., Boschetti, L., Roy, D. P., Humber, M. L., & Justice, C. O. (2018). The Collection 6 MODIS burned area mapping algorithm and product. *Remote Sensing of Environment*, *217*, 72–85. https://doi.org/10.1016/J.RSE.2018.08.005

Gorelick, N., Hancher, M., Dixon, M., Ilyushchenko, S., Thau, D., & Moore, R. (2017). Google Earth Engine: Planetary-scale geospatial analysis for everyone. *Remote Sensing of Environment*, *202*, 18–27. https://doi.org/10.1016/J.RSE.2017.06.031

Guo, Z., Wu, L., Huang, Y., Guo, Z., Zhao, J., & Li, N. (2022). Water-Body Segmentation for SAR Images: Past, Current, and Future. *Remote Sensing*, *14*(7), 1752. https://doi.org/10.3390/rs14071752

He, K., Zhang, X., Ren, S., & Sun, J. (2016). Deep residual learning for image recognition. *Proceedings of the IEEE Computer Society Conference on Computer Vision and Pattern Recognition*, *2016-Decem*, 770–778. https://doi.org/10.1109/CVPR.2016.90

Hu, A., & Demir, I. (2021). Real-time flood mapping on client-side web systems using hand model. *Hydrology*, *8*(2), 65. https://doi.org/10.3390/hydrology8020065

Hu, T., Hu, Y., Dong, J., Qiu, S., & Peng, J. (2021). Integrating Sentinel-1/2 Data and Machine Learning to Map Cotton Fields in Northern Xinjiang, China. *Remote Sensing 2021, Vol. 13, Page 4819*, *13*(23), 4819. https://doi.org/10.3390/RS13234819

Huang, Z., Pan, Z., & Lei, B. (2020). What, Where, and How to Transfer in SAR Target Recognition Based on Deep CNNs. *IEEE Transactions on Geoscience and Remote Sensing*, *58*(4), 2324–2336. https://doi.org/10.1109/TGRS.2019.2947634

Jafarzadegan, K., & Merwade, V. (2017). A DEM-based approach for large-scale floodplain mapping in ungauged watersheds. *Journal of Hydrology*, *550*, 650–662. https://doi.org/10.1016/j.jhydrol.2017.04.053

Jafarzadegan, K., & Merwade, V. (2019). Probabilistic floodplain mapping using HAND-based statistical approach. *Geomorphology*, *324*, 48–61. https://doi.org/10.1016/J.GEOMORPH.2018.09.024

Jain, P., Schoen-Phelan, B., & Ross, R. (2020). Tri-band assessment of multi-spectral satellite data for flood detection. *CEUR Workshop Proceedings*, *2766*. http://ceur-ws.org/Vol-2766/paper8.pdf

Jiang, W., Ni, Y., Pang, Z., Li, X., Ju, H., He, G., Lv, J., Yang, K., Fu, J., & Qin, X. (2021). An effective water body extraction method with new water index for sentinel-2 imagery. *Water (Switzerland)*, *13*(12), 1647. https://doi.org/10.3390/w13121647

Katiyar, V., Tamkuan, N., & Nagai, M. (2021). Near-real-time flood mapping using off-the-shelf models with sar imagery and deep learning. *Remote Sensing*, *13*(12), 2334. https://doi.org/10.3390/rs13122334

Konapala, G., Kumar, S. V., & Khalique Ahmad, S. (2021). Exploring Sentinel-1 and Sentinel-2 diversity for flood inundation mapping using deep learning. *ISPRS Journal of Photogrammetry and Remote Sensing*, *180*, 163–173. https://doi.org/10.1016/J.ISPRSJPRS.2021.08.016

Krajewski, W. F., Ghimire, G. R., Demir, I., & Mantilla, R. (2021). Real-time streamflow forecasting: AI vs. Hydrologic insights. *Journal of Hydrology X*, *13*, 100110. https://doi.org/10.1016/j.hydroa.2021.100110

Kseňak, Ľ., Pukanská, K., Bartoš, K., & Blišťan, P. (2022). Assessment of the Usability of SAR and Optical Satellite Data for Monitoring Spatio-Temporal Changes in Surface Water: Bodrog River Case Study. *Water (Switzerland)*, *14*(3), 299. https://doi.org/10.3390/w14030299

Lee, J. Sen, Ainsworth, T. L., & Wang, Y. (2017). A review of polarimetric SAR speckle filtering. *International Geoscience and Remote Sensing Symposium (IGARSS)*, *2017-July*, 5303–5306. https://doi.org/10.1109/IGARSS.2017.8128201

Li, H., Wang, C., Cui, Y., & Hodgson, M. (2021). Mapping salt marsh along coastal South Carolina using U-Net. *ISPRS Journal of Photogrammetry and Remote Sensing*, *179*, 121–132. https://doi.org/10.1016/j.isprsjprs.2021.07.011

Li, L., Yan, Z., Shen, Q., Cheng, G., Gao, L., & Zhang, B. (2019). Water body extraction from very high spatial resolution remote sensing data based on fully convolutional networks. *Remote Sensing*, *11*(10),

1162. https://doi.org/10.3390/rs11101162
Li, Y., Martinis, S., Plank, S., & Ludwig, R. (2018). An automatic change detection approach for rapid flood mapping in Sentinel-1 SAR data. *International Journal of Applied Earth Observation and Geoinformation*, *73*, 123–135. https://doi.org/10.1016/J.JAG.2018.05.023
Li, Z., & Demir, I. (2022). A comprehensive web-based system for flood inundation map generation and comparative analysis based on height above nearest drainage. *Science of The Total Environment*, *828*, 154420. https://doi.org/10.1016/J.SCITOTENV.2022.154420
Li, Z., Mount, J., & Demir, I. (2022). Accounting for uncertainty in real-time flood inundation mapping using HAND model: Iowa case study. *Natural Hazards*, *112*(1), 977–1004. https://doi.org/10.1007/S11069-022-05215-Z
Liu, B., Li, X., & Zheng, G. (2019). Coastal Inundation Mapping From Bitemporal and Dual-Polarization SAR Imagery Based on Deep Convolutional Neural Networks. *Journal of Geophysical Research: Oceans*, *124*(12), 9101–9113. https://doi.org/10.1029/2019JC015577
Liu, Q., Huang, C., Shi, Z., & Zhang, S. (2020). Probabilistic river water mapping from Landsat-8 using the support vector machine method. *Remote Sensing*, *12*(9), 1374. https://doi.org/10.3390/RS12091374
Liu, Y. (2018). *Height Above Nearest Drainage (HAND) for CONUS | CUAHSI HydroShare*. https://doi.org/Liu, Y. (2018). Height Above Nearest Drainage (HAND) for CONUS, HydroShare, https://doi.org/10.4211/hs.69f7d237675c4c73938481904358c789
Loey, M., Manogaran, G., Taha, M. H. N., & Khalifa, N. E. M. (2021). Fighting against COVID-19: A novel deep learning model based on YOLO-v2 with ResNet-50 for medical face mask detection. *Sustainable Cities and Society*, *65*, 102600. https://doi.org/10.1016/j.scs.2020.102600
Lu, J., Giustarini, L., Xiong, B., Zhao, L., Jiang, Y., & Kuang, G. (2014). Automated flood detection with improved robustness and efficiency using multi-temporal SAR data. *Remote Sensing Letters*, *5*(3), 240–248. https://doi.org/10.1080/2150704X.2014.898190
Manavalan, R. (2017). SAR image analysis techniques for flood area mapping - literature survey. *Earth Science Informatics*, *10*(1), 1–14. https://doi.org/10.1007/S12145-016-0274-2/FIGURES/8
Markert, K. N., Markert, A. M., Mayer, T., Nauman, C., Haag, A., Poortinga, A., Bhandari, B., Thwal, N. S., Kunlamai, T., Chishtie, F., Kwant, M., Phongsapan, K., Clinton, N., Towashiraporn, P., & Saah, D. (2020). Comparing Sentinel-1 Surface Water Mapping Algorithms and Radiometric Terrain Correction Processing in Southeast Asia Utilizing Google Earth Engine. *Remote Sensing 2020, Vol. 12, Page 2469*, *12*(15), 2469. https://doi.org/10.3390/RS12152469
Martinis, S., Kuenzer, C., Wendleder, A., Huth, J., Twele, A., Roth, A., & Dech, S. (2015). Comparing four operational SAR-based water and flood detection approaches. *International Journal of Remote Sensing*, *36*(13), 3519–3543. https://doi.org/10.1080/01431161.2015.1060647
Mignot, E., & Dewals, B. (2022). Hydraulic modelling of inland urban flooding: recent advances. *Journal of Hydrology*, 127763. https://doi.org/10.1016/j.jhydrol.2022.127763
Mishra, B., Dahal, A., Luintel, N., Shahi, T. B., Panthi, S., Pariyar, S., & Ghimire, B. R. (2022). Methods in the spatial deep learning: current status and future direction. *Spatial Information Research*, *30*(2), 215–232. https://doi.org/10.1007/S41324-021-00425-2/FIGURES/3
Moharrami, M., Javanbakht, M., & Attarchi, S. (2021). Automatic flood detection using sentinel-1 images on the google earth engine. *Environmental Monitoring and Assessment*, *193*(5), 1–17. https://doi.org/10.1007/S10661-021-09037-7/FIGURES/14
Molin, R. D., Rosa, R. A. S., Bayer, F. M., Pettersson, M. I., & Machado, R. (2019). A change detection algorithm for SAR images based on logistic regression. *International Geoscience and Remote Sensing Symposium (IGARSS)*, *2019-July*, 1514–1517. https://doi.org/10.1109/IGARSS.2019.8900064
Moothedan, A. J., Thakur, P. K., Garg, V., Dhote, P. R., Aggarwal, S. P., & Mohapatra, M. (2020). *Automatic Flood Mapping Using Sentinel-1 Grd Sar Images And Google Earth Engine: A Case Study Of Darbhangah, Bihar "RS-GIS Applications in HydroMeteorological Disaster Management-One Day online Workshop" 15 May, 2018 View project PSInSAR Study of Lyngenfj*. https://www.researchgate.net/publication/343539830

Muste, M., Lyn, D. A., Admiraal, D., Ettema, R., Nikora, V., & García, M. H. (2017). *Experimental Hydraulics: Methods, Instrumentation, Data Processing and Management: Volume I: Fundamentals and Methods*. CRC Press. https://www.google.com/books/edition/Experimental_Hydraulics_Methods_Instrume/YDgPEAAAQBAJ

NASA. (n.d.). *Central US Flooding and Storms Spring 2019 | NASA Applied Science*. Retrieved March 23, 2022, from https://appliedsciences.nasa.gov/what-we-do/disasters/disasters-activations/central-us-flooding-and-storms-spring-2019

Nobre, A. D., Cuartas, L. A., Hodnett, M., Rennó, C. D., Rodrigues, G., Silveira, A., Waterloo, M., & Saleska, S. (2011). Height Above the Nearest Drainage - a hydrologically relevant new terrain model. *Journal of Hydrology*, *404*(1–2), 13–29. https://doi.org/10.1016/j.jhydrol.2011.03.051

Oh, S., Jung, J., Shao, G., Shao, G., Gallion, J., & Fei, S. (2022). High-Resolution Canopy Height Model Generation and Validation Using USGS 3DEP LiDAR Data in Indiana, USA. *Remote Sensing*, *14*(4), 935. https://doi.org/10.3390/rs14040935

Papaioannou, G., Vasiliades, L., Loukas, A., & Aronica, G. T. (2017). Probabilistic flood inundation mapping at ungauged streams due to roughness coefficient uncertainty in hydraulic modelling. *Advances in Geosciences*, *44*, 23–34. https://doi.org/10.5194/ADGEO-44-23-2017

Pike, R., Goeller, N., Goetz, J., & Crookshanks, S. (2019). Key Planning Questions to Consider in Small Stream Hydrometric Monitoring. *Confluence: Journal of Watershed Science and Management*, *3*(2), 2. https://doi.org/10.22230/jwsm.2019v3n2a25

Potapov, P., Li, X., Hernandez-Serna, A., Tyukavina, A., Hansen, M. C., Kommareddy, A., Pickens, A., Turubanova, S., Tang, H., Silva, C. E., Armston, J., Dubayah, R., Blair, J. B., & Hofton, M. (2021). Mapping global forest canopy height through integration of GEDI and Landsat data. *Remote Sensing of Environment*, *253*, 112165. https://doi.org/10.1016/J.RSE.2020.112165

Quan, K. A. C., Nguyen, V. T., Nguyen, T. C., Nguyen, T. V, & Tran, M. T. (2020). Flood level prediction via human pose estimation from social media images. *ICMR 2020 - Proceedings of the 2020 International Conference on Multimedia Retrieval*, 479–485. https://doi.org/10.1145/3372278.3390704

Rambour, C., Audebert, N., Koeniguer, E., Le Saux, B., Crucianu, M., & Datcu, M. (2020). FLOOD DETECTION in TIME SERIES of OPTICAL and SAR IMAGES. *International Archives of the Photogrammetry, Remote Sensing and Spatial Information Sciences - ISPRS Archives*, *43*(B2), 1343–1346. https://doi.org/10.5194/isprs-archives-XLIII-B2-2020-1343-2020

Rennó, C. D., Nobre, A. D., Cuartas, L. A., Soares, J. V., Hodnett, M. G., Tomasella, J., & Waterloo, M. J. (2008). HAND, a new terrain descriptor using SRTM-DEM: Mapping terra-firme rainforest environments in Amazonia. *Remote Sensing of Environment*, *112*(9), 3469–3481. https://doi.org/10.1016/j.rse.2008.03.018

Ronneberger, O., Fischer, P., & Brox, T. (2015). U-net: Convolutional networks for biomedical image segmentation. *Lecture Notes in Computer Science (Including Subseries Lecture Notes in Artificial Intelligence and Lecture Notes in Bioinformatics)*, *9351*, 234–241. https://doi.org/10.1007/978-3-319-24574-4_28

Sadiq, R., Akhtar, Z., Imran, M., & Ofli, F. (2022). Integrating remote sensing and social sensing for flood mapping. *Remote Sensing Applications: Society and Environment*, *25*, 100697. https://doi.org/10.1016/j.rsase.2022.100697

Salehi, B., Mahdianpari, M., Amani, M., M. Manesh, F., Granger, J., Mahdavi, S., & Brisco, B. (2018). A Collection of Novel Algorithms for Wetland Classification with SAR and Optical Data. In *Wetlands Management - Assessing Risk and Sustainable Solutions*. https://doi.org/10.5772/intechopen.76596

Salluri, D. K., Bade, K., & Madala, G. (2020). Object detection using convolutional neural networks for natural disaster recovery. *International Journal of Safety and Security Engineering*, *10*(2), 285–291. https://doi.org/10.18280/ijsse.100217

Samela, C., Troy, T. J., & Manfreda, S. (2017). Geomorphic classifiers for flood-prone areas delineation for data-scarce environments. *Advances in Water Resources*, *102*, 13–28.

https://doi.org/10.1016/j.advwatres.2017.01.007
Scott, C. P., Beckley, M., Phan, M., Zawacki, E., Crosby, C., Nandigam, V., & Arrowsmith, R. (2022). Statewide USGS 3DEP Lidar Topographic Differencing Applied to Indiana, USA. *Remote Sensing*, *14*(4), 847. https://doi.org/10.3390/rs14040847
Segarra, J., Buchaillot, M. L., Araus, J. L., & Kefauver, S. C. (2020). Remote Sensing for Precision Agriculture: Sentinel-2 Improved Features and Applications. *Agronomy 2020, Vol. 10, Page 641*, *10*(5), 641. https://doi.org/10.3390/AGRONOMY10050641
Seo, B. C., Keem, M., Hammond, R., Demir, I., & Krajewski, W. F. (2019). A pilot infrastructure for searching rainfall metadata and generating rainfall product using the big data of NEXRAD. *Environmental Modelling and Software*, *117*, 69–75. https://doi.org/10.1016/j.envsoft.2019.03.008
Shen, X., Anagnostou, E. N., Allen, G. H., Robert Brakenridge, G., & Kettner, A. J. (2019). Near-real-time non-obstructed flood inundation mapping using synthetic aperture radar. *Remote Sensing of Environment*, *221*, 302–315. https://doi.org/10.1016/j.rse.2018.11.008
Sit, M., Demiray, B., & Demir, I. (2021). *Short-term Hourly Streamflow Prediction with Graph Convolutional GRU Networks*. https://doi.org/10.48550/arxiv.2107.07039
Sit, M., Seo, B.-C., & Demir, I. (2021). *IowaRain: A Statewide Rain Event Dataset Based on Weather Radars and Quantitative Precipitation Estimation*. https://doi.org/10.48550/arxiv.2107.03432
Tamiminia, H., Salehi, B., Mahdianpari, M., Quackenbush, L., Adeli, S., & Brisco, B. (2020). Google Earth Engine for geo-big data applications: A meta-analysis and systematic review. *ISPRS Journal of Photogrammetry and Remote Sensing*, *164*, 152–170. https://doi.org/10.1016/J.ISPRSJPRS.2020.04.001
Teague, A., Sermet, Y., Demir, I., & Muste, M. (2021). A collaborative serious game for water resources planning and hazard mitigation. *International Journal of Disaster Risk Reduction*, *53*, 101977. https://doi.org/10.1016/j.ijdrr.2020.101977
Tiampo, K., Woods, C., Huang, L., Sharma, P., Chen, Z., Kar, B., Bausch, D., Simmons, C., Estrada, R., Willis, M., & Glasscoe, M. (2021). A Machine Learning Approach to Flood Depth and Extent Detection Using Sentinel 1A/B Synthetic Aperture Radar. *Proceedings of the 2011 IEEE International Conference on Robotics and Biomimetics*, 558–561. https://doi.org/10.1109/igarss47720.2021.9553601
Tiwari, V., Kumar, V., Matin, M. A., Thapa, A., Ellenburg, W. L., Gupta, N., & Thapa, S. (2020). Flood inundation mapping- Kerala 2018; Harnessing the power of SAR, automatic threshold detection method and Google Earth Engine. *PLOS ONE*, *15*(8), e0237324. https://doi.org/10.1371/JOURNAL.PONE.0237324
Tsyganskaya, V, Martinis, S., Twele, A., Cao, W., Schmitt, A., Marzahn, P., & Ludwig, R. (2016). A fuzzy logic-based approach for the detection of flooded vegetation by means of synthetic aperture radar data. *International Archives of the Photogrammetry, Remote Sensing and Spatial Information Sciences - ISPRS Archives*, *41*, 371–378. https://doi.org/10.5194/isprsarchives-XLI-B7-371-2016
Tsyganskaya, Viktoriya, Martinis, S., Marzahn, P., & Ludwig, R. (2018). Detection of temporary flooded vegetation using Sentinel-1 time series data. *Remote Sensing*, *10*(8), 1286. https://doi.org/10.3390/rs10081286
Twele, A., Cao, W., Plank, S., & Martinis, S. (2016). Sentinel-1-based flood mapping: a fully automated processing chain. *International Journal of Remote Sensing*, *37*(13), 2990–3004. https://doi.org/10.1080/01431161.2016.1192304
USGS. (n.d.). *USGS 3DEP National Map Seamless 1/3 Arc-Second (10m)*. Retrieved March 23, 2022, from https://developers.google.com/earth-engine/datasets/catalog/USGS_3DEP_10m?hl=en#citations
Uuemaa, E., Ahi, S., Montibeller, B., Muru, M., & Kmoch, A. (2020). Vertical accuracy of freely available global digital elevation models (Aster, aw3d30, merit, tandem-x, srtm, and nasadem). *Remote Sensing*, *12*(21), 1–23. https://doi.org/10.3390/rs12213482
Verma, U., Chauhan, A., Manohara, M. P., & Pai, R. (2021). DeepRivWidth : Deep learning based semantic segmentation approach for river identification and width measurement in SAR images of Coastal Karnataka. *Computers and Geosciences*, *154*, 104805.

https://doi.org/10.1016/j.cageo.2021.104805
Wang, J., Wang, S., Wang, F., Zhou, Y., Wang, Z., Ji, J., Xiong, Y., & Zhao, Q. (2022). FWENet: a deep convolutional neural network for flood water body extraction based on SAR images. *International Journal of Digital Earth*, *15*(1), 345–361. https://doi.org/10.1080/17538947.2021.1995513
Wang, R. (2018). "Big Data of Urban Flooding: Dance with Social Media, Citizen Science, and Artificial Intelligence." *Geophysical Research Abstracts*, *20*, 2018–2404. https://ui.adsabs.harvard.edu/abs/2018EGUGA..20..404W/abstract
Wieland, M., Martinis, S., & Li, Y. (2019). Semantic segmentation of water bodies in multi-spectral satellite images for situational awareness in emergency response. *International Archives of the Photogrammetry, Remote Sensing and Spatial Information Sciences - ISPRS Archives*, *42*(2/W16), 273–277. https://doi.org/10.5194/isprs-archives-XLII-2-W16-273-2019
WMO. (2015). *World Hydrological Cycle Observing System Guidelines*. *1155*, 87. http://www.wmo.int/pages/
Wong, C. J., James, D., Besar, N. A., Kamlun, K. U., Tangah, J., Tsuyuki, S., & Phua, M. H. (2020). Estimating Mangrove above-ground biomass loss due to deforestation in Malaysian Northern Borneo between 2000 and 2015 using SRTM and landsat images. *Forests*, *11*(9), 1018. https://doi.org/10.3390/F11091018
Xiang, Z., Demir, I., Mantilla, R., & Krajewski, W. F. (2021). *A Regional Semi-Distributed Streamflow Model Using Deep Learning*. https://doi.org/10.31223/X5GW3V
Xu, C., Zhang, S., Zhao, B., Liu, C., Sui, H., Yang, W., & Mei, L. (2021). SAR image water extraction using the attention U-net and multi-scale level set method: flood monitoring in South China in 2020 as a test case. *Geo-Spatial Information Science*. https://doi.org/10.1080/10095020.2021.1978275
Xu, H., Demir, I., Koylu, C., & Muste, M. (2019). A web-based geovisual analytics platform for identifying potential contributors to culvert sedimentation. *Science of The Total Environment*, *692*, 806–817. https://doi.org/10.1016/J.SCITOTENV.2019.07.157
Xu, H., Muste, M., & Demi, I. (2019). Web-based geospatial platform for the analysis and forecasting of sedimentation at culverts. *Journal of Hydroinformatics*, *21*(6), 1064–1081. https://doi.org/10.2166/HYDRO.2019.068
Xu, Q., Yuan, X., Ouyang, C., & Zeng, Y. (2020). Attention-based pyramid network for segmentation and classification of high-resolution and hyperspectral remote sensing images. *Remote Sensing*, *12*(21), 1–34. https://doi.org/10.3390/rs12213501
Yan, C., Fan, X., Fan, J., & Wang, N. (2022). Improved U-Net Remote Sensing Classification Algorithm Based on Multi-Feature Fusion Perception. *Remote Sensing*, *14*(5), 1118. https://doi.org/10.3390/rs14051118
Yan, K., Di Baldassarre, G., Solomatine, D. P., & Schumann, G. J. P. (2015). A review of low-cost space-borne data for flood modelling: topography, flood extent and water level. *Hydrological Processes*, *29*(15), 3368–3387. https://doi.org/10.1002/HYP.10449
Yang, Q., Shen, X., Anagnostou, E. N., Mo, C., Eggleston, J. R., & Kettner, A. J. (2021). A High-Resolution Flood Inundation Archive (2016–the Present) from Sentinel-1 SAR Imagery over CONUS. *Bulletin of the American Meteorological Society*, *102*(5), E1064–E1079. https://doi.org/10.1175/BAMS-D-19-0319.1
Ye, K., Wang, Z. z., Yu, Y., & Li, Z. (2021). Rapid monitoring and analysis of Weihui flood using Sentinel-1A SAR data. *International Conference on Environmental Remote Sensing and Big Data (ERSBD 2021)*, *12129*(9), 18. https://doi.org/10.1117/12.2625585
Yildirim, E., & Demir, I. (2021). An Integrated Flood Risk Assessment and Mitigation Framework: A Case Study for Middle Cedar River Basin, Iowa, US. *International Journal of Disaster Risk Reduction*, *56*, 102113. https://doi.org/10.1016/j.ijdrr.2021.102113
Zhang, H., Liu, M., Wang, Y., Shang, J., Liu, X., Li, B., Song, A., & Li, Q. (2021). Automated delineation of agricultural field boundaries from Sentinel-2 images using recurrent residual U-Net. *International Journal of Applied Earth Observation and Geoinformation*, *105*, 102557. https://doi.org/10.1016/j.jag.2021.102557

Zhang, W., Hu, B., & Brown, G. S. (2020). Automatic surface water mapping using polarimetric SAR data for long-term change detection. *Water (Switzerland), 12*(3), 872. https://doi.org/10.3390/w12030872